The Mass-Conservative Cell-Integrated Semi-Lagrangian Advection Scheme on the Sphere

RAMACHANDRAN D. NAIR

Department of Marine, Earth, and Atmospheric Sciences, North Carolina State University, Raleigh, North Carolina

BENNERT MACHENHAUER

Climate Research Division, Danish Meteorological Institute, Copenhagen, Denmark

(Manuscript received 16 February 2001, in final form 13 August 2001)

ABSTRACT

A mass-conservative cell-integrated semi-Lagrangian (CISL) scheme is presented and tested for 2D transport on the sphere. The total mass is conserved exactly and the mass of each individual grid cell is conserved in general. The scheme is based on a general scheme developed by Machenhauer and Olk that has increased cost effectiveness without loss of accuracy, compared to the CISL scheme of Rančić. A regular latitude–longitude grid is used on the sphere and upstream trajectories from the corner points of the regular grid cells (the Eulerian cells) define the corner points of the departure cells. The sides in these so-called Lagrangian cells are generally defined as straight lines in a (λ, μ) plane, where λ is the longitude and μ is the sine of the latitude. The mass distribution within each Eulerian grid cell is defined by quasi-biparabolic functions, which are used to integrate analytically the mass in each Lagrangian computational cell. The auxiliary computational cells are polygons with each side parallel to the coordinate axis. Also, the computational cells have the same area as the Lagrangian cells they approximate. They were introduced in order to simplify the analytical integrals of mass. Near the poles, the east and west sides of certain Lagrangian cells cannot be approximated by straight lines in the (λ, μ) plane, and are instead represented by straight lines in polar tangent plane coordinates. Each of the latitudinal belts of Lagrangian cells in the polar caps are split up into several latitudinal belts of subcells, which can be approximated by computational cells as in the case of cells closer to the equator. One latitudinal belt in each hemisphere, which encloses the Eulerian pole (singular belt), is treated in a special way. First the total mass in the singular belt is determined and then it is redistributed among the cells in the belt using weights determined by a traditional SL scheme at the midpoints of the cells. By this procedure the total mass is still conserved while the conservation is only approximately maintained for the individual cells in the singular belt. These special treatments in the polar caps fit well into the general structure of the code and can be implemented with minor modifications in the code used for the rest of the sphere.

Compared to two other conservative advection schemes implemented on the sphere the CISL scheme used here was found to be competitive in terms of accuracy for the same resolution. In addition the CISL scheme has the advantage over these schemes that it is applicable for Courant numbers larger than one. In plane geometry the scheme of Rančić had an overhead factor of 2.5 in CPU time compared to a traditional bicubic semi-Lagrangian scheme. This factor is reduced to 1.1 for the Machenhauer and Olk scheme on the plane while on the sphere the factor is found to be 1.28 for the present scheme. This overhead seems to be a reasonable price to pay for increased accuracy and exact mass conservation.

1. Introduction

In recent years, the use of semi-Lagrangian (SL) advection methods in numerical weather prediction (NWP) models has become very popular. Compared to Eulerian algorithms, SL methods allow for relatively long time steps, decreasing the computational time required for the completion of numerical forecasts. As a result, it has been adopted as the basis for high-resolution operational NWP models (Ritchie et al. 1995; Côté et al. 1998) and is being tested for use in climate models (Williamson and Olson 1998). The SL advection offers additional advantages beyond the longer time step. It gives minimal phase error, minimizes the computational disperson, and can handle sharp discontinuities. Also, efficient monotonic and positive-definite short-wave filters can be easily incorporated into SL advection schemes (Nair et al. 1999a). However, a serious disadvantage of SL schemes in operational use is that they do not formally conserve integral invariants as total mass (Laprise and Plante 1995; Moorthi et al. 1995). A

Corresponding author address: Dr. Bennert Machenhauer, Danish Meteorological Institute, Lyngbyvej 100, DK-2100 Copenhagen OE, Denmark.
E-mail: bm@dmi.dk

posteriori correction is often needed to enforce conservation of such quantities.

The SL transport algorithm is very attractive mainly due to its significant computational efficiency. Therefore, it is desirable to exploit the efficiency of SL schemes in computationally intensive climate and atmospheric chemistry models. For pollution transport models and climate models, numerical conservation properties are very important. Various methods have been devised to make conventional SL schemes mass conserving, but such methods require frequent ad hoc mass restoration (e.g., Priestly 1993; Gravel and Staniforth 1994). However such a posteriori mass fixing after the upstream interpolation is not only computationally expensive but also has a great deal of arbitrariness present in the process, as pointed out by Machenhauer and Olk (1997). Leslie and Purser (1995) have developed 3D mass-conserving SL schemes employing forward trajectories based on so-called cascade interpolation for limited area models. Rančić (1992, 1995) and Laprise and Plante (1995) developed mass-conservative SL algorithms on the 2D Cartesian plane, based on the cell-integrated SL method employing a piecewise parabolic method (PPM) of Colella and Woodward (1984). Extension of these methods in spherical geometry (global domain) is a challenge because of the polar singularities.

There are only a few conservative transport schemes available for spherical geometry application. Smolarkiewicz and Rasch (1991) have used a conservative Eulerian scheme on a sphere with a very high computational cost. Rasch (1994) developed a scheme and demonstrated its application on a *reduced* spherical grid. Li and Chang (1996) developed a conservative scheme in spherical geometry adopting the approaches of Prather (1986) and Bott (1993). Lin and Rood (1996, hereafter referred to as LR96) and Rasch (1998) developed accurate multidimensional schemes from a 1D finite-volume-based scheme and applied them to spherical geometry. Unfortunately these schemes too have time step restrictions; that is, the meridional Courant number must satisfy $C_\theta \leq 1$. Very recently Hourdin and Armenguad (1999) have reviewed conservative 1D finite-volume-based global schemes, and presented tests of 3D advection using time splitting, that is, 1D advection done sequentially in the three coordinate directions of a global GCM.

In the present study, a scheme for 2D advection on the sphere based on the so-called cell-integrated semi-Lagrangian (CISL) scheme developed by Machenhauer and Olk (1996, 1998), is proposed. This is a mass-conserving CISL advection scheme based on a 2D representation (quasi-biparabolic), and applicable without time splitting and the Courant number restriction. A perspective for the future is a consistent extension of the present scheme to a conservative 3D advection scheme, which may be applied in all the advection terms in a primative equations (PE) numerical model (Machenhauer and Olk 1998) combined with the semi-implicit time-stepping scheme (Machenhauer and Olk 1997). In the present study, however, we focus on the development and test the performance of the scheme for 2D advection only.

In section 2, we describe the PPM used for the present study. In section 3 the CISL remapping scheme is described. Extension of the CISL method in spherical geometry is given in section 4. Numerical experiments to test the accuracy and efficiency of the scheme are presented in section 5. Summary and conclusions are presented in Section 6.

2. Application of the PPM to SL schemes

The piecewise parabolic method of representation is becoming popular in meteorological modeling (Carpenter et al. 1990; Rančić 1992; Laprise and Plante 1995; Machenhauer and Olk 1996, 1998). The PPM was used originally in a finite-volume scheme developed by Colella and Woodward (1984), which uses the average value of the grid zones rather than the gridpoint values. This ''cell integrated'' scheme is inherently mass conservative and the monotonic or positive-definite option can be easily incorporated into it (Carpenter et al. 1990). Rančić (1992) developed a cell-integrated PPM-based SL advection scheme in 2D Cartesian geometry. This is a 2D extension of the Colella and Woodward (1984) scheme in a semi-Lagrangian context.

In the traditional SL scheme employing backward trajectories, the arrival points are assumed to be regular grid points, and the estimated values of the field at a new time level are computed at the upstream departure points by means of a suitable interpolation. However, in the finite-volume-based SL methods (hereafter referred to as CISL methods), the scalar fileds (or densities) that are to be advected are the *average* values over cell areas with known corner points (grid points). The SL time discretization implies that the value of the advected field at a new time level is just the average value of the *departure* cell defined by the upstream positions (trajectory origins) corresponding to the arrival cell's corner grid points. Laprise and Plante (1995) discuss both upstream and downstream variants of CISL methods. In the present study, however, we use only the upstream variant of a CISL method.

We call the arrival cells Eulerian cells and the departure (or upstream) cells Lagrangian cells. The Eulerian cell walls are defined by grid lines while the Lagrangian cell walls are defined by specified curves connecting the departure points of the Eulerian cell corner points. These curves must approach grid lines when the velocities, determining the corner point trajectories, approach zero. For an orthogonal 2D Cartesian grid system the Eulerian walls are straight lines and consequently the Lagrangian walls are specified as straight lines too. Thus the Eulerian cells are rectangles and the Lagrangian cells may be considered quadrilaterals. Machenhauer and Olk (1997) examined the stability of the CISL

scheme in a 1D case. For a stable and conservative solution, it is necessary to choose the time step Δt in such a way that the trajectories do not cross intersect. This is analogous to the Lipschitz criterion for stability in the case of the traditional SL advection scheme (Smolarkiewicz and Pudykiewicz 1992). Moreover for 2D advection, this condition implies that the line segments forming the cell do not cross (Scroggs and Semazzi 1995); that is, the areas of the Lagrangian cells should be *well defined.* The CISL scheme has essentially two basic steps. First, parabolic profiles are fitted within each Eulerian cell using the cell average values. The second step consists of determining the mass (density) enclosed in each Lagrangian cell by analytically integrating the parabolas over the Lagrangian cell area; this step is often called remapping (Dukowicz 1984).

a. Parabolic representation of cells in 1D

First we consider the 1D case of the CISL scheme and further it will be extended to 2D, including spherical geometry. A parabola in any Eulerian cell can be uniquely defined as

$$h(x) = h_0 + h_1 x + h_2 x^2, \tag{1}$$

where h_0, h_1, and h_2 are the coefficients of the parabola, and x is a normalized local variable such that

$$x \in [-1/2, +1/2].$$

Let $\overline{h}$ be the cell-averaged density defined by

$$\overline{h} = \int_{-1/2}^{+1/2} h(x)\, dx, \tag{2}$$

and let $h_L = h(-1/2)$ and $h_R = h(1/2)$ be the left and right cell boundary (edge) values, respectively, which are cubically interpolated from the given neighboring cell-averaged densities (Colella and Woodward 1984). Then the parabola is determined in such a way that it fits the boundary values and fulfills (2). With these constraints the density distribution function $h(x)$ can be represented as follows:

$$h(x) = \overline{h} + \delta h x + h_S\left(\frac{1}{12} - x^2\right), \tag{3}$$

where for convenience we have introduced the derived coefficients,

$$\delta h = h_R - h_L, \qquad h_S = 6\overline{h} - 3(h_L + h_R).$$

These coefficients can be further modified to make monotonic or positive-definite versions of $h(x)$. In the present study, we use such filtering constraints as suggested by Carpenter et al. (1990) and LR96.

b. Cell representation in 2D

Rančić (1992) showed that the CISL method can be applied for conservative transport in a 2D context, by introducing a biparabolic function to represent the distribution of density in each Eulerian cell. A biparabolic function is a direct extension of (1) in 2D, with nine coefficients. Computation of these nine coefficients can be very expensive. However, we use a ''quasi-biparabolic'' function (4) with only five coefficients to represent the mass distribution in each cell. This can significantly reduce the computational cost of the remapping procedure (section 3) by simplifying the area integrals involved in the 2D remapping scheme. Although formally only second-order accurate in the two coordinate directions, our results show that the quasi-biparabolic function still yields a very accurate representation. Another advantage is that the quasi-biparabolic representation in each cell may be easily modified to be monotonic and/or positive definite.

The quasi-biparabolic function representing an Eulerian cell can be written in normalized local (x, y) coordinates as

$$h(x, y) = \overline{h} + a^x x + b^x\left(\frac{1}{12} - x^2\right) + a^y y + b^y\left(\frac{1}{12} - y^2\right), \tag{4}$$

where

$$x, y \in [-1/2, 1/2],$$

$\overline{h}$ is the average value in the cell, and (a^x, b^x) and (a^y, b^y) are coefficients of the parabola in the x and the y direction, respectively. Note that the above 2D parabolic function needs only two 1D parabolic fits to determine the coefficients. These coefficients are defined as in the 1D case, and may be further modified for either the monotonic or positive-definite option in the respective two coordinate directions. Moreover, with this definition of $h(x, y)$, it can be easily shown that the surface integral of the density distribution function over the cell is equal to the cell-average value ($\overline{h}$):

$$\int_{-1/2}^{1/2}\int_{-1/2}^{1/2} h(x, y)\, dx\, dy = \overline{h}.$$

3. The CISL remapping

Mass enclosed in the Lagrangian cells can be determined using a remapping technique (Dukowicz 1984). This is the most important computational aspect of a CISL method. In the 1D case remapping is not a difficult task; however, in 2D, remapping can be difficult as the Lagrangian cells are arbitrary quadrilaterals formed on the domain spanned by regular Eulerian cells. Rančić (1992), Laprise and Plante (1995), Scroggs and Semazzi (1995), and Machenhauer and Olk (1998) have developed different remapping methods in 2D. Rančić (1995) and LR96 have extended the 1D remapping schemes into 2D with a dimension-splitting approach.

In order to formulate the conservative CISL scheme, here we consider the differential form of the continuity equation:

$$\frac{\partial \rho}{\partial t} + \nabla \cdot \rho \mathbf{V} = 0, \tag{5}$$

where ρ is the density and $\mathbf{V}$ is the velocity vector. When integrating (5) over a time-dependent Lagrangian volume $V(t)$, that is, a volume of the fluid enclosed by a material boundary surface moving with the fluid, we get the following integral form of the continuity equation:

$$\frac{d}{dt} \int_{V(t)} \rho \, dV = 0, \tag{6}$$

where d/dt is the total (Lagrangian) derivative. The integral in (6) represents the mass of a particle enclosed in $V(t)$ and thus (6) states that mass of an individual particle is conserved along its trajectory. Note that instead of integrating over a Lagrangian volume, if we integrate (5) over the total volume considered, which we assume has fixed closed boundaries, then the result is also an equation of the form (6). In this case it states that the total mass is conserved. Here, by fixed closed boundaries we mean a time-dependent boundary surface with no inflow or outflow of mass, as in the following applications.

When integrating (6) over a time step, Δt, along a trajectory of the fluid particle, we get the following two-time-level SL scheme:

$$\int_{V(t^{n+1})} \rho \, dV = \int_{V(t^n)} \rho \, dV, \tag{7}$$

where $t^n = n\Delta t$ and $t^{n+1} = (n + 1)\Delta t$ are the current and the unspecified future time of the advection step, respectively. By defining the volume-average density to be

$$\overline{\rho} = \frac{1}{V} \int_V \rho \, dV, \tag{8}$$

(7) can be written as

$$\overline{\rho}^{n+1} V^{n+1} = \overline{\rho}^n V^n, \tag{9}$$

where the superscripts n and $n + 1$ denote the departure (current) and arrival (future) time levels. In the following discussions, 1D and 2D versions of (9) will be considered for developing the CISL remapping algorithm.

a. The CISL scheme in 1D

First we consider the 1D CISL advection scheme introduced by Machenhauer and Olk (1996, 1998) to illustrate the remapping algorithm, in a two-time-level context. Figure 1 schematically illustrates the CISL advection in the 1D case. Assume that the arrival points are regularly spaced Eulerian grid points $x_{j\pm1/2}$ at time $t + \Delta t$ (or time level $n + 1$), and corresponding departure points are the irregularly spaced Lagrangian points $x^*_{j\pm1/2}$ at time t (or time level n). In Fig. 1, the Eulerian and Lagrangian points are marked by open squares and filled circles, respectively. Let $\Delta x_j = (x_{j+1/2} - x_{j-1/2})$ be the grid spacing (cell width) of the Eulerian grid and let the corresponding Lagrangian grid spacing be $\Delta x^*_j = (x^*_{j+1/2} - x^*_{j-1/2})$. With this spatial discretization, let $h^n_j(x)$ be the known density distribution at the time level n, of the jth Eulerian cell. Then the cell-average density (mass per unit length) $\overline{h}^{n+1}_j$ of the arrival cell defined by Δx_j at the new time level $n + 1$ can be determined by using the 1D equivalent to (9):

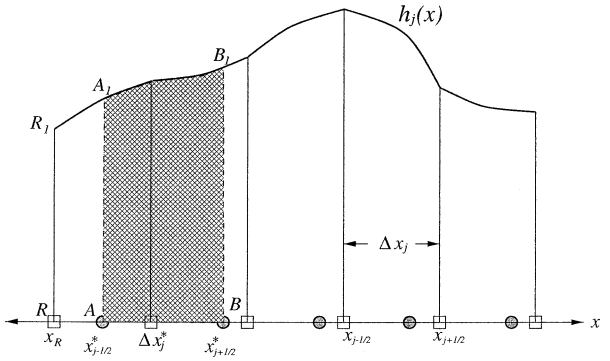

FIG. 1. Schematic diagram illustrating the remapping scheme used for CISL advection in the 1D case, where $x_{j\pm1/2}$ denote regular Eulerian grid points (open squares) and the corresponding Lagrangian grid points (filled circles) are denoted by $x^*_{j\pm1/2}$. The density distribution in the domain is represented by piecewise parabolas, and $h_j(x)$ is the parabolic representation of the density distribution in an Eulerian cell defined by Δx_j. The density in the corresponding Lagrangian cell is represented by the parabolic curves joining A_1 and B_1.

$$\overline{h}^{n+1}_j \Delta x_j = \overline{h}^*_j \Delta x^*_j, \tag{10}$$

where * denotes the upstream value evaluated at the known time level n and $\overline{h}^*$ is the integral mean value of the density distribution over the Lagrangian cell Δx^*_j; that is,

$$\overline{h}^*_j = \frac{1}{\Delta x^*_j} \int_{x^*_{j-1/2}}^{x^*_{j+1/2}} h^n_j(x) \, dx. \tag{11}$$

The density distributions $h^n_j(x)$ in Eulerian cells are often represented by piecewise polynomials (Bott 1993; Rasch 1994). Also the density across the cell walls is not necessarily continuous (Laprise and Plante 1995). In the present study, we use the piecewise parabolic function (3) to represent the density distribution for each of the Eulerian cells. This representation is generally continuous across the cell walls. Thus, to determine the average density at the new time level $\overline{h}^{n+1}_j$, the rhs of (10) should be evaluated, which implies that the function (3) needs to be integrated (analytically) over the Lagrangian cell $[x^*_{j-1/2}, x^*_{j+1/2}]$ as shown in (11).

Geometric interpretation of the remapping is rather easy as illustrated in Fig. 1. The shaded region represents the mass in the Lagrangian cell (shown as area under the parabolic curves A_1B_1). It may be computed

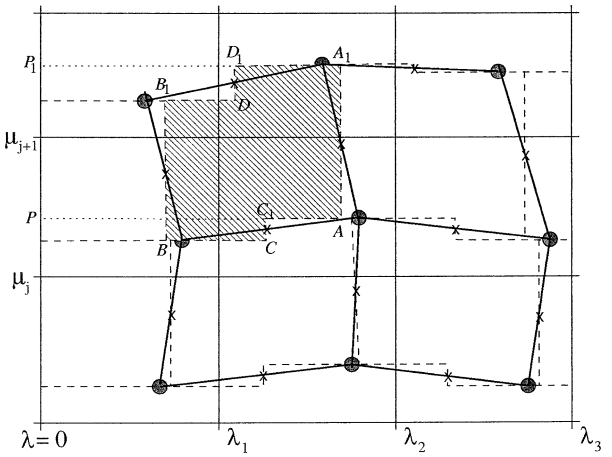

FIG. 2. Schematic illustration of the CISL remapping scheme in 2D, where the filled circles represent the Lagrangian grid points corresponding to the Eulerian grid points (grid intersections) in the (λ, μ) plane. The Lagrangian cells are approximated by polygons (computational cells) with sides (dashed lines) parallel to the λ or μ coordinate axis. The vertical sides of the polygons are constructed through the midpoints ($\times$) of the walls of the Lagrangian cells, and horizontal sides of the polygons pass through the Lagrangian points.

as the total accumulated mass toward the line $x = x^*_{j+1/2}$ from the common reference line in the left $x = x_R$ minus the accumulated mass toward the line $x = x^*_{j-1/2}$ from the reference line $x = x_R$. If we denote the total mass accumulated toward the line $x = x^*_{j+1/2}$from the reference line by $A(x^*_{j+1/2})$, then the mass in the Lagrangian cell is

$$\overline{h}^*_j \Delta x^*_j = A(x^*_{j+1/2}) - A(x^*_{j-1/2}).$$

Thus, the new cell-average value of density at the future time level, from (10), is

$$\overline{h}^{n+1}_j = \frac{1}{\Delta x_j}[A(x^*_{j+1/2}) - A(x^*_{j-1/2})]. \qquad (12)$$

On a uniform grid with a constant wind field, it can be shown that the process of parabolic representation of density distribution in Eulerian cells, followed by upstream estimation of density at Lagrangian cells, is formally *equivalent* to an SL scheme with cubic interpolation at upstream points (Laprise and Plante 1995).

b. The CISL remapping in 2D

We use a fully 2D remapping rather than using a dimension-splitting approach (Rančić 1995). Figure 2 schematically illustrates our CISL scheme in 2D with (λ, μ) as Cartesian coordinates. The filled circles are the upstream Lagrangian points corresponding to the Eulerian grid (thin lines) intersections. The Lagrangian cell walls are shown as thick lines with midpoints marked by $\times$s.

The upstream Lagrangian cells are generally quadrilaterals with irregularly oriented sides, and the computation of the exact mass enclosed in such cells is a complicated task, which we want to simplify for the sake of efficiency. Following Machenhauer and Olk (1998), first we approximate the Lagrangian cells by ''computational cells,'' which are polygons with sides parallel to the coordinate axis λ or μ. Each computational cell is constructed so that it has the same area as the Lagrangian cell it approximates. In Fig. 2 the sides of the computational cells are shown as dashed lines, for convenience we consider a particular computational cell bounded by the polygon $BCC_1AA_1D_1DB_1B$ (the shaded region). The vertical sides (or walls) of the computational cells are constructed with lines through the midpoints ($\times$) of the Lagrangian cell walls and lines along the horizontal sides pass through the Lagrangian points (here, on a map with north upward, ''vertical'' and ''horizontal'' lines means lines oriented north–south and east–west, respectively). In general, the computational cell (polygon) has eight sides; however, in certain special cases it can have fewer sides. Thus in Fig. 2, the shaded polygon approximates the Lagrangian cell in question, and mass computed in the polygon approximates that in the Lagrangian cell.

The entire closed domain can be filled with such polygons without any overlaps or cracks (disjoint regions), which ensures exact total mass conservation. Now we discuss mass computation in the shaded polygon $BCC_1AA_1D_1DB_1B$ using the 2D remapping scheme. Let $\lambda = 0$ be the common reference line (Fig. 2), from which accumulated mass is computed toward each vertical side of the computational cell. Thus, the mass enclosed (M_C) in the shaded polygon is

$$M_C = M_S(AA_1) - M_S(BB_1) + M_S(CC_1) - M_S(DD_1), \qquad (13)$$

where M_S denotes the mass in the rectangular region from the reference line to the specified vertical segment (see Fig. 3 for details).

Generally, the first, second, third, and fourth terms are the accumulated masses toward those sides that end up in the east, west, south, and north sides, respectively. However, to be valid in general the accumulated masses in Eq. (13) must be determined with signs, positive or negative, which depend on the orientation of the Lagrangian cell sides in question. The accumulated masses to be substituted into (13) with the right signs are determined by expressions introduced in the next subsection. Equation (13) may be used as a general formula for determining the mass in a particular cell. As in the case of the Lagrangian cells, the computational cells also share their boundary walls with their neighbors, and therefore it is only necessary to find the accumulated mass corresponding to the east and the south walls of each of the Lagrangian cells, while computing from west to east and south to north.

As seen from Fig. 2, the accumulated mass $M_S(AA_1)$ is equal to the accumulated west-side mass $M_S(BB_1)$ for the neighboring cell located to the west of the current

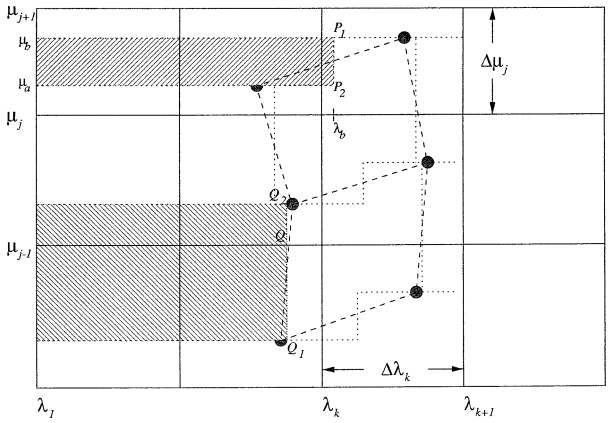

FIG. 3. Schematic illustration of the mass accumulated from the vertical reference line $\lambda = \lambda_1$ to the computational cell wall P_1P_2 [$M_S(P_1P_2)$], represented by the upper shaded stripe. If a stripe is separated by a grid line (bottom stripe), then accumulated mass is computed for each individual stripe and added, i.e., $M_S(Q_1Q_2) = M_S(Q_1Q) + M_S(QQ_2)$.

cell, and $M_S(CC_1)$ is equal to the accumulated north-side mass $M_S(DD_1)$ for the neighboring cell south of the current cell. Thus, using Eq. (13) while stepping through the grid, one just adds the accumulated masses $M_S(AA_1)$ and $M_S(CC_1)$ to the current cell, and subtracts the same amount, respectively, from the neighbor to the east and the neighbor to the south.

c. Determination of the accumulated mass

In 2D, (9) can be written as follows:

$$\overline{h}^{n+1}\Delta A = \overline{h}^{*}\Delta A^{*}, \tag{14}$$

where ΔA is the area of the arrival cell at the future time $t + \Delta t$ and ΔA^* is the area of the upstream Lagrangian cell at time t. In order to predict the value of the average density (mass per unit area) $\overline{h}^{n+1}$ at the future time level $n + 1$, the quantity $\overline{h}^{*}\Delta A^*$ in (14) should be known. In other words, we need to evaluate the following integral:

$$\overline{h}^{*}\Delta A^{*} = \iint_{\Delta A^*} h^n(\lambda, \mu)\, d\lambda\, d\mu, \tag{15}$$

where $h^n(\lambda, \mu)$ is the known density distribution at the time level n. First, we represent $h^n(\lambda, \mu)$ in each Eulerian cell by the quasi-biparabolic function (4), introduced in the previous section. Trajectory origins corresponding to the Eulerian cell's corner points are then determined, and straight lines joining these points define the Lagrangian cell with area ΔA^*. Mass enclosed in the actual Lagrangian cells is finally approximated by that in the computational cells, using the 2D remapping scheme (13). The accumulated masses toward the computational cell walls remain to be estimated.

Computational cells by design are made of rectangular regions. We refer to each of the rectangular regions from the reference line (usually left border of the domain) to a cell wall as a stripe. Thus, accumulated mass toward any computational cell wall, for example, AA_1, (Fig. 2) is the total mass in the stripe PP_1A_1A. Figure 3 shows different formations of stripes (shaded regions). Now, we discuss the computation of accumulated mass toward a cell wall (or the total mass in a stripe). Consider the upper stripe in Fig. 3, bounded by the region $[\lambda_a, \lambda_b] \otimes [\mu_a, \mu_b]$, then the mass M_S in that stripe is

$$M_S = \int_{\lambda_a}^{\lambda_b}\int_{\mu_a}^{\mu_b} h(\lambda, \mu)\, d\lambda\, d\mu, \tag{16}$$

where $h(\lambda, \mu)$ is the density distribution function in the domain (for ease of notation, the dependence of the function on time index n is suppressed). Let $\lambda_a = \lambda_1$ be the reference line and

$$\lambda_b \in [\lambda_k, \lambda_{k+1}], \qquad \mu_a, \mu_b \in [\mu_j, \mu_{j+1}]$$

as shown in Fig. 3. Using the properties of a definite integral, (16) can now be written as

$$M_S = \sum_{i=1}^{k-1}\int_{\lambda_i}^{\lambda_{i+1}}\int_{\mu_a}^{\mu_b} h_{ij}(\lambda, \mu)\, d\lambda\, d\mu + \int_{\lambda_k}^{\lambda_b}\int_{\mu_a}^{\mu_b} h_{kj}(\kappa, \mu)\, d\lambda\, d\mu, \tag{17}$$

where $h_{ij}(\lambda, \mu)$ is the piecewise quasi-biparabolic function representing the density distribution at each Eulerian cell C_{ij}.

Here an Eulerian grid cell is characterized by two indices increasing in the positive direction of the λ and μ axes, respectively. The cell indices are also used for the southwestern corner point. We use the convention that the indices of a Lagrangian (departure) point are the same as those of the corresponding Eulerian (arrival) point. From Eq. (16) it is seen that the sign of M_S depends on the sign of $\mu_b - \mu_a$. In order to get the right signs of the accumulated masses to be used in Eq. (13) for the cell (i, j), we must, according to the above conventions, for a south wall, use $\mu_a = \mu_{i,j}$ and $\mu_b = \mu_{i+1,j}$. In the case of an east wall we must use $\mu_a = \mu_{i,j+1}$ and $\mu_b = \mu_{i+1,j+1}$.

For convenience we now introduce the local (x, y) coordinate system for each Eulerian cell C_{ij} such that

$$x = \frac{\lambda - \lambda_i}{\Delta\lambda_i} - \frac{1}{2} \quad \text{and} \quad y = \frac{\mu - \mu_j}{\Delta\mu_j} - \frac{1}{2},$$

where $\Delta\lambda_i = \lambda_{i+1} - \lambda_i$ and $\Delta\mu_j = \mu_{j+1} - \mu_j$. For each left and right grid point $\lambda = \lambda_i$ and $\lambda = \lambda_{i+1}$, we have $x = -1/2$ and $x = 1/2$, respectively. Let $[y_a, y_b]$ be the values corresponding to $[\mu_a, \mu_b]$ and x_b be the value corresponds to λ_b in (x, y) coordinates, respectively, so that, x_a, x_b, y_a, and $y_b \in [-1/2, 1/2]$. Now (17) can be modified for the evaluation of accumulated mass toward a cell wall P_1P_2 (Fig. 3) as follows:

$$M_S(P_1P_2) = \sum_{i=1}^{k-1} \Delta\lambda_i \Delta\mu_j \int_{-1/2}^{1/2} \int_{y_a}^{y_b} h_{ij}(x, y)\, dx\, dy + \Delta\lambda_k \Delta\mu_j \int_{-1/2}^{x_b} \int_{y_a}^{y_b} h_{kj}(x, y)\, dx\, dy. \quad (18)$$

The quasi-biparabolic function (4) for any cell C_{ij} can be expressed as

$$h_{ij}(x, y) = f_{ij}^x(x) + f_{ij}^y(y), \quad (19)$$

where

$$f_{ij}^y(y) = \overline{h}_{ij} + a_{ij}^y y + b_{ij}^y \left[\frac{1}{12} - y^2\right] \quad \text{and}$$

$$f_{ij}^x(x) = a_{ij}^x x + b_{ij}^x \left[\frac{1}{12} - x^2\right].$$

Substituting (19) into (18) and simplifying, we get

$$M_S(P_1P_2) = \int_{y_a}^{y_b} \left[H_{ij} + A_{ij}^y y + B_{ij}^y \left(\frac{1}{12} - y^2\right)\right] dy + \Delta\lambda_k \Delta\mu_j \left[(y_b - y_a) \int_{-1/2}^{x_b} f_{kj}^x\, dx + \left(x_b + \frac{1}{2}\right) \int_{y_a}^{y_b} f_{kj}^y\, dy\right], \quad (20)$$

where

$$H_{kj} = \sum_{i=1}^{k-1} \Delta\lambda_i \Delta\mu_j \overline{h}_{ij}, \qquad A_{kj}^y = \sum_{i=1}^{k-1} \Delta\lambda_i \Delta\mu_j a_{ij}^y, \quad \text{and}$$

$$B_{kj}^y = \sum_{i=1}^{k-1} \Delta\lambda_i \Delta\mu_j b_{ij}^y$$

are the ''accumulated coefficients.''

Thus, to determine the accumulated mass at the Lagrangian cell walls, at each time step, it is necessary to know three accumulated coefficients for each cell in addition to the five coefficients of the quasi-biparabolic function (4). The integral (20) can be analytically integrated and may further be derived for efficient numerical evaluation. Also, (20) is designed for nonuniform resolution grids. The stripe bounded by the rectangle $\mu_a P_2 P_1 \mu_b$ in Fig. 3 may be considered as an *elementary* stripe. Any other formation of the stripes can be split into such elementary stripes and accumulated mass can be estimated. For example, if the stripe is separated by a grid line (bottom stripe shown in Fig. 3), then the accumulated mass for each stripe above and below the grid line of separation, the sum of which is the total accumulated mass, can be determined individually. The remapping calculation is inherently asymmetrical with respect to the two coordinate directions. However, this has only a negligible impact, at least for remapping in a Cartesian grid. Tests have shown only negligible differences between the results obtained with masses accumulated in either the λ or the μ direction (Machenhauer and Olk 1998).

4. Extension to spherical geometry

Extension of CISL methods to spherical geometry is not straightforward due to polar singularities. A special treatment is needed in polar caps to obviate the pole problems, as is also done in the conservative Eulerian advection schemes of Rasch (1994), Li and Chang (1996) and LR96.

The time discretization (9) form of the Lagrangian derivative on a spherical surface domain may be written as in (14)

$$\overline{h}^{n+1} \Delta A = \overline{h}^* \Delta A^*, \quad (21)$$

where ΔA and ΔA^* are arrival cell area at time $t + \Delta t$ and corresponding Lagrangian cell area at time t, respectively, on the surface of the sphere. The mass in the Lagrangian cell is

$$\overline{h}^* \Delta A^* = a^2 \iint_{\Delta A^*} h^n(\lambda, \theta) \cos\theta\, d\lambda\, d\theta, \quad (22)$$

where λ and θ are the longitude and latitude, respectively; a is the radius of the sphere; and $h^n(\lambda, \theta)$ is the known density distribution function at the time level n. Also, $\lambda \in [0, 2\pi]$ and $\theta \in [-\pi/2, \pi/2]$.

The integral (22) can be simplified by introducing the independent variable $\mu = \sin\theta$ such that $\mu \in [-1, 1]$. By virtue of this substitution the integral in (22) transforms to an integral in the Cartesian (λ, μ) system and (22) becomes

$$\overline{h}^* \Delta A^* = a^2 \iint_{\Delta A^*} h^n(\lambda, \mu)\, d\lambda\, d\mu. \quad (23)$$

The above equation, except for the factor a^2, is formally similar to (16). Therefore, we can use the same procedures as those described for the Cartesian 2D case; that is, the integral in (22) is evaluated as $a^2 M_C$, where M_C is determined by (13).

At first, however, the Eulerian and corresponding Lagrangian cells must be defined on the (λ, μ) plane. On the sphere we use a spherical coordinate grid, which is equidistant in latitude and longitude, that is, with uniform grid spacing $(\Delta\lambda, \Delta\theta)$. By the transformation from the spherical coordinate system to the (λ, μ) system, the equidistant latitude–longitude grid transforms into a grid with straight coordinate grid lines. In the (λ, μ) plane the longitudes (λ grid lines) remain equidistant, while the latitudes (μ grid lines) become increasingly compressed toward the poles and thus become nonequidistant. Both pole points become straight lines, $\mu = \pm 1$. Therefore, in the (λ, μ) plane, as in the plane case, all the Eulerian cell walls are straight grid lines.

As in the plane case (except near the poles) we define the Lagrangian cell walls as straight lines connecting the departure points of the Eulerian cell corner points and find that generally the Lagrangian cells are quadrilaterals. Again if the velocities, determining the corner point trajectories of a cell, are zero, that is, there is no movement of the cell, then the straight Lagrangian cell walls are identical to the straight Eulerian cell walls, as required for consistency.

As the mapping of an area on the sphere to the (λ, μ) plane is area preserving ($a^2 \cos\theta d\lambda d\theta = a^2 \Delta\lambda \Delta\mu$), areas on the globe may be evaluated by integration over the corresponding areas in the (λ, μ)plane. With these properties and definitions the remapping procedures described in the previous section for the plane 2D case can be used. However, certain special treatments have to be introduced. In section 4b we specify special treatments that are needed for the Lagrangian cells near the Eulerian poles. These, special treatments are needed because of the convergence of the latitudes and the singularities at the polar lines in the (λ, μ) plane. In addition, due to the periodic boundary condition in the zonal direction, special treatment is required for cells that are separated by the reference line $\lambda = 0$. This problem is dealt with in section 4c.

a. The CISL scheme in the polar regions

In the spherical latitude–longitude coordinate system, the north–south Lagrangian cell walls should be great circle segments to be consistent with the form of the Eulerian cells. Such Lagrangian cell walls would appear as straight-line segments in the (λ, μ) coordinate system over the regions away from pole lines. However, near a pole line in the (λ, μ) plane the north–south cell walls would be curved, and the curvature would increase as the lines move toward the pole (see Fig. 4a). Thus, a straight-line segment (wall) in the polar zones of the (λ, μ) plane will not be a true image of the great circle segment representing north–south wall in the latitude–longitude system. Therefore, the choice of straight-line segments as the north–south walls for the Lagrangian cells in the polar zones is not accurate and this may adversely affect the local mass conservation. In order to circumvent this deficiency, we need to consider a local tangent plane coordinate system, where straight-line segments are good approximations for the north–south walls of the Lagrangian cells. Note that the east–west walls of the Lagrangian cells in the latitude–longitude coordinate system near the polar zones are well represented by straight lines in the corresponding (λ, μ) system. This is mainly because the lengths of these sides become very small near the polar zones in both coordinate systems, and any deviation from the actual east–west sides has only a negligible effect on the cell area.

We introduce two tangent plane coordinate systems, one tangent to the north pole and the other one tangent to the south pole, both with the origin at the pole point. They are both polar systems with the polar angle equal to λ and the polar radius $r = \sqrt{2(1 - \mu)}$ in the north pole system and $r = \sqrt{2(1 + \mu)}$ in the south pole system. Note that transformations between the spherical coordinate system and both tangent plane systems are area-preserving $d\lambda d\mu = \mp r dr d\lambda$. For the north pole system the corresponding rectangular coordinates are

$$X = \sqrt{2(1 - \mu)} \cos\lambda, \quad \text{and} \tag{24}$$

$$Y = \sqrt{2(1 - \mu)} \sin\lambda, \tag{25}$$

and for the south polar region the tangent plane coordinates are given by

$$X = \sqrt{2(1 + \mu)} \cos\lambda, \quad \text{and} \quad Y = \sqrt{2(1 + \mu)} \sin\lambda.$$

Then the corner points of a Lagrangian cell near the poles can be expressed in terms of (X, Y) in the respective tangent planes.

It is possible to compute analytically in these tangent plane coordinate systems the accumulated mass for a strip from the reference line $\lambda = 0$ toward a straight line connecting two east-side corner points. This would be the most ideal procedure. However, for simplicity, here we introduce an approximate procedure. In the polar regions where the east cell sides in the (λ, μ) system, which correspond to the straight cell sides in the tangent plane system, are strongly curved lines, they are treated as piecewise straight lines by the introduction of additional points along the curved sides. Thus, all the straight east cell sides in a polar latitude cell row on the tangent plane are divided into a certain number of equal pieces by auxiliary points (X_p, Y_p). These points are then transformed to the (λ, μ) coordinate system using

→

FIG. 4. (a) (top) Schematic illustration of straight-line segments P_0P_1, P_0P_2, P_0P_3, and P_0P_4 in a polar tangent (X, Y) plane and (bottom) the corresponding transformed curves in the (λ, μ) plane; P_0 is the Lagrangian pole point and the line segments represent sides in two Lagrangian cells in a singular belt. (b) Schematic illustration of the singular belt (shaded region) as projected onto a polar stereographic plane. The regular latitudes and longitudes are denoted by dashed circles and straight lines, respectively. The Lagrangian latitudes and longitudes are shown as ellipses and smooth curves, respectively. The Eulerian pole is marked by a filled circle and the corresponding Lagrangian pole is marked by an open square. (c) Schematic diagram showing the ''singular belt'' (shaded region) in the (λ, μ) plane. The thick curves are the Lagrangian latitudes corresponding to the thin μ-grid lines. The point marked by $\times$ denotes the Lagrangian pole point corresponding to the Eulerian pole line defined by $\mu = 1$. The upstream Lagrangian points (cell corner points) are marked by open circles; see the text for further details.

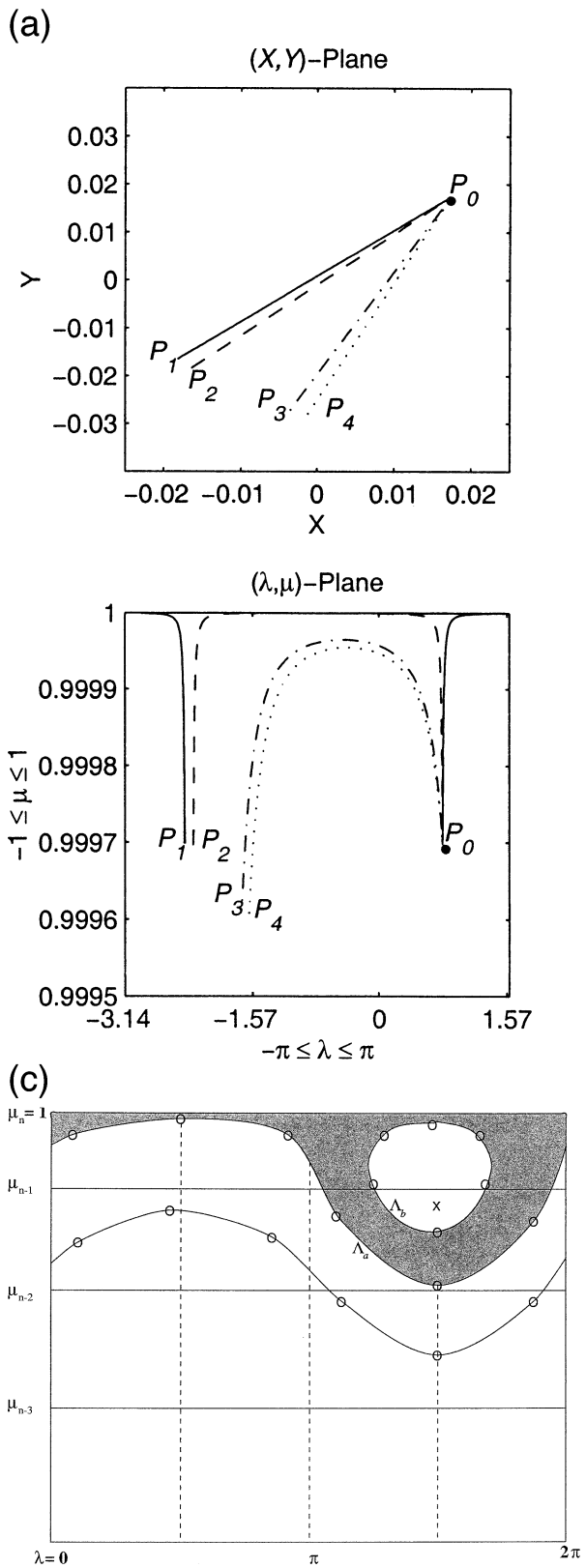
(a)
(X,Y)−Plane
0.03
0.02
0.01
0
−0.01
−0.02
−0.03
Y
P0
P1
P2
P3
P4
−0.02 −0.01 0 0.01 0.02
X
(λ,μ)−Plane
1
0.9999
0.9998
0.9997
0.9996
0.9995
−1 ≤ μ ≤ 1
P1
P2
P3
P4
P0
−3.14 −1.57 0 1.57
−π ≤ λ ≤ π
(b)
(c)
μn= 1
μn-1
μn-2
μn-3
Λb
x
Λa
λ= 0
π
2π

$$\lambda_p = \tan^{-1}(Y_p/X_p), \quad \text{and} \tag{26}$$

$$\mu_p = 1 - (X_p^2 + Y_p^2)/2 \tag{27}$$

for the north pole region [for the south pole region λ_p is given as in (26) and the corresponding $\mu_p = (X_p^2 + Y_p^2)/2 - 1$]. Here, they are treated as corner points in auxiliary subcells. The latitude cell row in question is thus divided into a certain number of rows of subcells with straight east cell sides. Therefore, the remapping of these subcell rows can be done exactly as for the nondivided cell rows outside the polar regions, with only small modifications in the code.

b. *Estimation of mass in the polar "singular" regions*

In general the Lagrangian cells or subcells are quadrilaterals in the (λ, μ) plane with well-defined cell sides as specified in the preceding subsections. Exceptions are the two Lagrangian cells, which include an Eulerian pole, that is, the north pole or the south pole. As an example, Fig. 4a shows schematically such a cell including the north pole, in the upper figure in the tangent plane and in the lower figure in the (λ, μ) plane. The cell in question is denoted by $P_0P_1P_2$. Also shown is a Lagrangian cell $P_0P_3P_4$ in the same latitudinal row. Because the cell sides are so close to the Eulerian pole the east and west cell sides are very much curved in the (λ, μ) plane and would require the addition of several auxiliary points in order to be approximated well by piecewise straight-line segments. Furthermore, it is evident that the usual remapping procedure will not work for the cell including the pole point as it is not a closed quadrilateral in the (λ, μ) plane. Therefore, some special treatment would be required for the pole-point cell and in addition all the cells in the same latitude row would have to be divided into several subcells. This could be done, but it would, respectively, complicate the programming and decrease somewhat the efficiency of the whole advection scheme. Instead we test here a simple, approximate method that fits well into the general program structure. We call the degenerated polar cells "singular cells" and call an array of cells along the latitude circles that includes a singular cell a "singular belt." Our approximate method retains the conservation of mass for the whole singular belt but treats only approximately the conservation for each individual cell in the belt. Figure 4b schematically shows the singular belt (shaded region) on a tangent plane. The dashed circles are regular latitudes, and the longitudes are denoted by dashed straight lines. The corresponding Lagrangian latitudes are shown as ellipses and longitudes as thin straight lines. The Eulerian pole is marked by a filled circle, and the corresponding Lagrangian pole is marked by an open square.

Without loss of generality, we may consider a solid-body rotation case on the sphere (Williamson et al. 1992) to illustrate the computational procedure. Figure 4c schematically shows the distribution of Lagrangian points in the (λ, μ) plane, for such a case when the wind flow is along the pole-to-pole direction. In the figure the Lagrangian pole is denoted as $\times$ and located in the second row of Eulerian cells from the pole line (i.e., the directional Courant number along the longitudes, $1 < C_\theta \leq 2$). The thick curves are the Lagrangian latitudes on which the cell corner points are marked by open circles. We have seen that for the singular cell (in the shaded region) the mass cannot be constructed using the regular approach. Nevertheless, for the last row of triangular Lagrangian cells with the Lagrangian pole point as the common corner point (Fig. 4b). In Fig 4c this belt is shown as a region bounded by the closed curve Λ_b enclosing the Lagrangian pole point), the computational cells can be constructed and the mass in the individual cells can be estimated in the usual ways.

For computational convenience, we determine the total mass in the singular belt and redistribute it for the constituent cells. We consider the north pole region bounded by the Lagrangian latitude Λ_a (Fig. 4c) and the pole line defined by $\mu = 1$. First, we construct an array of auxiliary cells by drawing lines parallel to the μ axis from the Lagrangian points on the lower boundary line (Λ_a) to the pole line. The computational cells corresponding to the new set of auxiliary cells can now be constructed and mass enclosed in each of such cells can be determined by the regular approach. Total mass bounded by the Lagrangian latitude (Λ_a) is then the sum of the masses in the constituent cells. Also the total mass in the closed region bounded by Λ_b containing the Lagrangian pole can be determined by the regular approach. Thus, the total mass in the singular belt is the difference between the total mass in the closed region bounded by Λ_b and the total mass in the region bounded by Λ_a. This idea can be further generalized for any $C_\theta > 1$, where inside the singular belt we may have concentric closed regions enclosing the Lagrangian pole. For the cases of $C_\theta \leq 1$, the singular belt does not contain the closed region bounded by Λ_b as shown in Fig. 4c, and in this case the mass in the region bounded by Λ_a gives the total mass in the singular belt.

The next step is to redistribute the total mass (T^M) in the singular belt for each of the constituent cells. We use a conventional SL method for finding the *weights* of redistribution. First, we estimate the coordinates of the cell centers for each of the cells in the singular belt on the tangent plane, for example, defined by (24) and (25), using the known (λ, μ) coordinates of the corner points. Then, the upstream values of the density, w_i, at these points are determined by employing the computationally efficient quasi-bicubic interpolation (Ritchie et al. 1995).

The mass in the Lagrangian cell C_i^M is then given by

$$C_i^M = T^M \frac{|w_i|}{\sum_i |w_i|}, \tag{28}$$

such that $\Sigma_i C_i^M = T^M$. The absolute values of the weights are used to avoid negative values.

c. Computational cells separated by the reference line

Accumulated mass is always determined from the common reference line, usually considered to be the west boundary wall of the computational domain. The (λ, μ) plane is east–west periodic and the longitude $\lambda = 0$ is a natural choice as a reference grid line. Since the domain is periodic, some of the computational cells may be separated by the vertical reference line. Near the polar regions the computational cells may be advected several grid lengths depending on the zonal wind velocity and may cross the reference line.

The remapping process (13) in such cells needs special attention, since the vertical walls of the computational cells may lie on either side of the reference line. There are many ways to solve this problem. We choose a simple approach described as follows. If a computational cell is separated by the reference line, then the accumulated mass (or the mass in the stripes) toward the vertical walls that appear to the right side of the reference line should be modified. This is done by adding the total mass in the stripes with the same width wrapping around the latitude circles, starting from the reference line and going to the reference line.

5. Numerical results

Different options of the CISL scheme have been tested in 1D and 2D Cartesian geometry. Since here we mainly focus on the spherical geometry application of the CISL scheme, these results are not presented. Here we consider two numerical experiments to test the CISL scheme in spherical geometry. These experiments are solid-body rotation of a passive scalar on the surface of the sphere and a deformation flow test for a time-dependent vortex simulated near the poles.

The scalar ψ used in the following advection tests is equal to the 2D density $h(\lambda, \mu)$ used in (14) and (21), that is, mass per unit area. Thus it could be the surface pressure divided by gravity (P_s/g) in a shallow water model. It could also be the pressure difference divided by gravity between the top and bottom of a model layer in a GCM, that is, $\psi = \Delta_k(P)/g$, as used by Machenhauer and Olk (1998), in their extension of the present 2D CISL scheme to 3D. In this extension ψ could additionally be the mass per unit area of any single atmospheric component in a GCM, for example, water vapor or a chemical constituent, in this case $\psi = q_k \Delta P/g$ where q_k is a specific measure of concentration of the component in question (mass of component per unit mass of moist air).

a. Solid-body rotation

Solid-body rotation is a commonly used experiment to test an advection scheme over the sphere. The details of the experiment are given in Williamson et al. (1992). We use the parameter values of the experiment setup as given in Williamson and Rasch (1989) and Nair et al. (1999b, hereafter referred to as NCS99).

The velocity components of the advecting wind field are given by

$$u = u_0(\cos\alpha \cos\theta + \sin\alpha \cos\lambda \sin\theta), \quad \text{and} \tag{29}$$

$$v = -u_0 \sin\alpha \sin\lambda, \tag{30}$$

where α is the angle between the axis of solid-body rotation and the polar axis of the spherical coordinate system (Williamson et al. 1992). The flow field is such that when $\alpha = 0$, the axis of rotation is the polar axis, and when $\alpha = \pi/2$, it is in the equatorial plane. The initial scalar distribution is assumed to be a cosine bell. Thus

$$\psi(\lambda, \theta) = \begin{cases} \frac{1}{2}\left[1 + \cos\left(\frac{\pi r'}{R}\right)\right], & \text{if } r' < R \\ 0, & \text{if } r' \geq R, \end{cases} \tag{31}$$

where

$$r' = \cos^{-1}[\sin\theta_c \sin\theta + \cos\theta_c \cos\theta \cos(\lambda - \lambda_c)] \tag{32}$$

is the great circle distance between (λ, θ) and the bell center, initially taken as $(\lambda_c, \theta_c) = (3\pi/2, 0)$. The bell radius R is set to $7\pi/64$ as in Rasch (1994), Li and Chang (1996), LR96, and NCS99. The analytic solution of the advection equation at any time step appears to be identical to the initial condition since the solid-body rotation translates the cosine bell around the globe without incurring any deformation of shape.

The spherical (λ, θ) domain consists of a 128×65 uniform-resolution (2.8125°) mesh, where the first and last latitudinal grid lines represent the south and the north poles, respectively. Thus, there are 128×64 grid cells spanning the entire spherical domain or the equivalent computational (λ, μ) plane. Note that the scalar field is initially determined as gridpoint values at the cell centers rather than being average values over the cells, as they should have been. The time step and the value of the maximum wind speed u_0 are chosen such that the angular velocity of the rotational flow is either $\omega = 2\pi/256$ or $\omega = 2\pi/72$ per time step. In these cases the meridional Courant number $C_\theta = 0.5$ or $C_\theta = 1.78$, and a complete revolution around the globe takes 256 or 72 time steps, respectively.

b. Results of solid-body rotation

Numerical experiments have been performed for $\alpha = 0$, $\pi/2 - 0.05$, and $\pi/2$ with exact trajectories as recommended by Williamson et al. (1992). Three different

options of the CISL scheme have been used, which are the monotonic option (CISL-M), the positive-definite option (CISL-P), and the CISL scheme without any filtering (CISL-N). In addition to that, a conventional SL scheme with bicubic-Lagrange interpolation (SL-BCL) has been used for comparison.

As discussed in section 4, to improve the local mass conservation, the Lagrangian cells in the polar regions are meridionally subdivided by introducing trajectory points along the east (or west) walls. However, the singular belt is excluded from such division and the total mass in this belt is estimated and redistributed to the constituent cells. For the present study, the three Lagrangian belts closest to the pole in each hemisphere have been ''refined'' by introducing additional points. We have done two sets of experiments, by introducing three, two, and one additional points (nonuniform refinement) along each east (or west) wall of the Lagrangian cells (starting closest to the pole) and another combination of two, two, and two (uniform refinement) points. The nonuniform refinements (three, two, and one) were found to be slightly more accurate than the uniform refinement. Also we have experimented with different combinations with more Lagrangian belts and additional points. There was no significant improvement in the results with *high-resolution* refinement of more belts and the above-mentioned combinations were found to be the most cost effective.

Results after one complete revolution around the globe (256 time steps) using the CISL-P and CISL-M schemes are displayed in Fig. 5, together with the analytic solution (dashed contours), where the contour values varies from 0.1 to 0.9 with uniform increments of 0.1. For this experiment we have used three, two, and one additional points on the north–south cell walls in the Lagrangian belts. The top panels in Fig. 5 are for polar flow with $\alpha = \pi/2$, while the bottom panels are for equatorial flow with $\alpha = 0$. Since the flow pattern of CISL-N is very similar to that of CISL-P, the corresponding figures of CISL-N are not shown. For the polar flow, the cosine bell has undergone a small stretching in the flow direction for CISL-P. When the flow is along the equator, the numerical solution obtained by using the CISL-P scheme is very close to the analytic solution. However in both cases the numerical solution with the CISL-M scheme is less accurate than that of CISL-P. Monotonicity constraints resulted in slight degradation of the shape of the cosine bell. Particularly in the central region (Fig. 5; CISL-M), the bell is stretched along the direction of the flow for both cases when $\alpha = \pi/2$ and $\alpha = 0$. Also, for the monotonic case, stretching of the central region of the cosine bell is visible in Fig. 14 of LR96.

Table 1 shows the normalized errors [for definition of error measures, see Williamson et al. (1992) and NCS99] for the solid-body rotation experiment with $\alpha = \pi/2$. Also for easy comparison, the results from similar case studies by LR96 and Rasch (1994) are provided in the same table. The error measures show that our results are comparable with the flux-form SL (FFSL) schemes of LR96 with monotonic [FFSL-5(M)] and positive definite constraints [FFSL-3(P)]. The CISL gives better accuracy in l_∞ (normalized maximum absolute error), maximum (normalized overshoot), and minimum (normalized undershoot) errors (monotonic case). However, the FFSL scheme has slightly smaller l_1 (normalized mean absolute error) and l_2 (normalized root mean square error) in both cases shown. Rasch (1994) developed a 2D forward-in-time upwind-biased flux-form scheme and extended it to the ''reduced spherical grid'' (RG2.8). Table 1 shows that both the CISL and the FFSL schemes are more accurate than Rasch's scheme.

Table 2 shows error measures for solid-body rotation along the equator ($\alpha = 0$) after one revolution or 256 time steps. Compared with the corresponding results in Table 1 the errors of the CISL-N and CISL-P schemes are consistently smaller for flow along the equator. This is in spite of much higher resolution in the zonal direction in the polar caps, which is in favor of the cross-pole experiments. It indicates that the special procedures introduced in the polar regions might be improved. In the case of the CISL-M scheme the errors are larger in Table 2 than in Table 1. This indicates that the error introduced by monotonization of the quasi-biparabolic function in this case dominates those introduced by the approximation in the polar caps.

Further, we have performed a series of polar flow tests with the CISL scheme to prove its robustness. Figure 6 shows a polar stereographic projection of the cosine bell advection at time steps 32, 64, and 96, as the bell approaches, passes over, and leaves the north pole, respectively. The bottom panel of Fig. 6 shows the cross polar simulation with the shift parameter $\alpha = \pi/2 - 0.05$. In both cases there is no visible distortion of the cosine bell as it passes over the pole. Moreover, Fig. 6 (top panel) is very similar to Fig. 13 of LR96. Time traces of l_1, l_2, and l_∞ for the CISL-P scheme with $\alpha = \pi/2$ are shown in Fig. 7. Here, error plots are more variable at time steps 64 and 192 (when the bell crosses the poles) with relatively large values for l_∞. However, the curves become again relatively smooth when the bell has crossed the poles. Compared to Figs. 7 and 8 of Rasch (1994), the maximum value of the time traces of error is much smaller with the CISL scheme.

In addition to the regular *slow* cross-polar advection test, we have done experiments with the *strong* flow. In this case 72 time steps are used for one revolution ($C_\theta = 1.78$) with $\alpha = \pi/2$. For this set of experiments we have used the uniform refinement for the polar Lagrangian belts. Figure 8 shows the position of the cosine bell near the north pole (top-left and -right panels) and over the south pole (bottom-left panel) and at the initial position (bottom-right panel) after 72 time steps (one revolution); the CISL-P scheme is used for the advection. There is no visible distortion for the cosine bell even

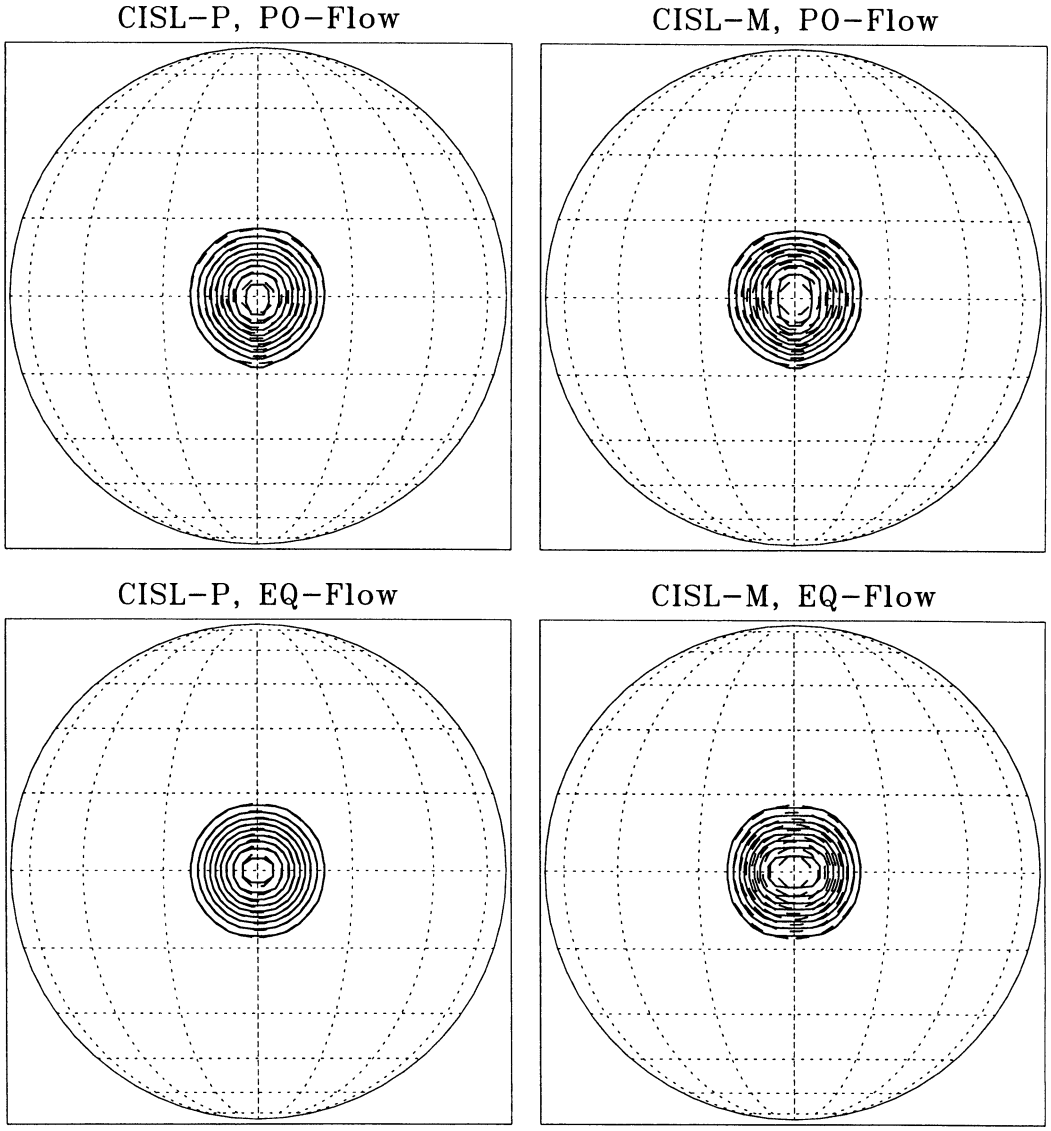

FIG. 5. Results on an orthographic projection of solid-body rotation of a cosine bell after one revolution (256 time steps). The CISL scheme with the positive-definite option (CISL-P) and the monotonic option (CISL-M) are used for the advection. (top left), (top right) The numerical solution with the CISL-P and the CISL-M scheme, respectively, when the flow is along the pole-to-pole direction ($\alpha = \pi/2$). (bottom left), (bottom right) The numerical solutions with CISL-P and CISL-M, respectively, when the flow is along the equator ($\alpha = 0$). The analytic solution is shown by dashed contours.

for the strong polar wind. After one revolution, the numerical solution appears to be very close to the analytic solution (dashed contours). Table 3 shows the standard errors for this particular test. For comparison, errors of regular SL advection with a bicubic-Lagrange interpolation (SL-BCL) are also listed. From this table it is evident that in addition to conserving the mass exactly, which the SL-BCL does not, the accuracy of the CISL scheme is superior to that of the SL-BCL scheme. Note that for this experiment the FFSL schemes of LR96 or Rasch's schemes could not be used since the meridional Courant number $C_\theta > 1$.

c. Deformational flow test

In order to compare the accuracy and robustness of the CISL scheme further with the conventional SL scheme, here we consider a deformation flow test in spherical geometry. NCS99 gives the details of the idealized vortex problem of Doswell (1984) on the surface of the sphere. The flow field is deformational and more challenging than the solid-body rotation. Here we use a different version of the vortex problem than that considered by NCS99. The flow field used here is positive definite, smooth, and the vortex is simulated on the sur-

TABLE 1. Error measures for solid-body rotation of a cosine bell for CISL schemes when the flow is along the pole-to-pole direction ($\alpha = \pi/2$) with 256 time steps for one revolution. The letters N, P, and M denote no filter, positive definite and monotonic options, respectively. For comparison, results of various published schemes are also presented; see text for the details.

Scheme	l_1	l_2	l_∞	Max	Min
CISL-N	0.063	0.046	0.048	−0.016	−0.0041
CISL-P	0.059	0.045	0.048	−0.016	−0.0034
CISL-M	0.084	0.084	0.109	−0.052	−0.0001
FFSL-5(P)	0.047	0.041	0.053	−0.053	−0.0013
FFSL-3(M)	0.078	0.079	0.124	−0.124	−0.0009
RG2.8	0.289	0.196	0.164	−0.150	−0.0271
RG2.8M	0.181	0.158	0.196	−0.210	0

face of the sphere rather than projected onto a polar tangent plane.

Let (λ', θ') be the rotated coordinate system with the north pole at (λ_0, θ_0) with respect to the regular spherical coordinate system (λ, θ). Consider the rotation of the (λ', θ') system with angular velocity ω' such that

$$\frac{d\lambda'}{dt} = \omega' \quad \text{and} \tag{33}$$

$$\frac{d\theta'}{dt} = 0. \tag{34}$$

In the case of the solid-body rotation test problems, the angular velocity ω' is a constant, but for the deformational problem we consider an ω' that varies with respect to the latitude θ'.

A steady circular vortex is defined to have normalized tangential velocity:

$$V_t = \frac{3\sqrt{3}}{2} \operatorname{sech}^2(\rho') \tanh(\rho'), \tag{35}$$

where $\rho' = r_0 \cos\theta'$ is the *radius* of the vortex and r_0 is a constant. The angular velocity is specified as

$$\omega'(\theta') = \begin{cases} 0 & \text{if } \rho' = 0, \\ \dfrac{V_t}{\rho'} & \text{if } \rho' \neq 0. \end{cases} \tag{36}$$

The analytical solution at time t is

$$\psi(\lambda', \theta', t) = 1 - \tanh\left[\frac{\rho'}{d} \sin(\lambda' - \omega' t)\right], \tag{37}$$

where d is the *smoothness* parameter for the flow field. The initial condition for the advected scalar is given by $\psi(\lambda', \theta', 0)$.

The exact upstream position of a particle at time t that arrives at a point (λ', θ') at time $t + \Delta t$ is given by

$$\lambda'(t) = \lambda'(t + \Delta t) - \omega' \Delta t, \tag{38}$$

$$\theta'(t) = \theta'(t + \Delta t). \tag{39}$$

How to specify the problem in the unrotated (λ, θ) coordinate system and the derivation of the components of velocity are described in NCS99.

TABLE 2. Error measures for solid-body rotation of a cosine bell for CISL schemes when the flow is along the equator ($\alpha = 0$) with 256 time steps for one revolution.

Scheme	l_1	l_2	l_∞	Max	Min
CISL-N	0.051	0.035	0.032	−0.015	0.0065
CISL-P	0.025	0.025	0.031	−0.014	0.0
CISL-M	0.094	0.091	0.108	−0.052	0.0

For the present study we have set the parameters $(\lambda_0, \theta_0) = (\pi + 0.025, \pi/2.2)$, $r_0 = 3$, and $d = 5$. With these conditions two symmetric vortices are created, one near the north pole and the other one near the south pole. The flow field is smooth, and the vortex centers are approximately at 81°N and 81°S. Also, this setup keeps the vortex centers away from the poles to avoid symmetry with the underlying spherical geometry. The point values of the initial field are generated at the cell centers on a 128 × 64 grid of cells, and integrated for three time units with 32 time steps. The corresponding Courant numbers in the λ and θ directions are $C_\lambda = 38.3$ and $C_\theta = 1.65$, respectively.

d. Results for the deformational flow test

Figure 9 (top-left panel) shows the initial conditions of the smooth scalar field and (top-right panel) the analytic solution after three time units. The bottom-left panel of Fig. 9 shows the numerical solution after 32 time steps with CISL-N, and the bottom-right panel shows the same with SL-BCL (without any filter). The shape of the vortex center is better captured by the CISL-N scheme as compared to the SL-BCL scheme. Table 4 shows that in addition to exact mass conservation the numerical solution of the CISL scheme is also more accurate. However the very small overshoots and undershoots, that is, the maximum and minimum errors, with the CISL scheme are slightly greater than the corresponding values of the SL-BCL scheme. The main reason for this difference is probably due to the truncation error involved in the difference process of the remapping scheme (13), where the mass in a computational cell is determined as the difference of accumulated masses.

6. Summary and conclusions

A mass-conservative cell-integrated semi-Lagrangian (CISL) scheme has been presented and tested for 2D transport on the sphere. This scheme is based on a general remapping scheme developed by Machenhauer and Olk (1996, 1997, 1998) and designed to be cost effective without loss of accuracy as compared to the CISL scheme of Rančić (1992). Here the 2D advection scheme is extended in a simple and cost-effective way to the spherical geometry by introducing special treatments near the poles. A regular latitude–longitude grid is used on the sphere and one-time-step upstream trajectories

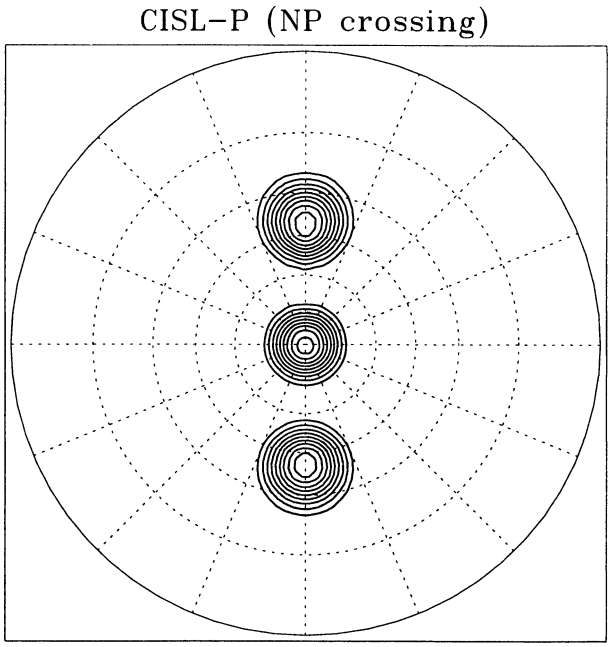

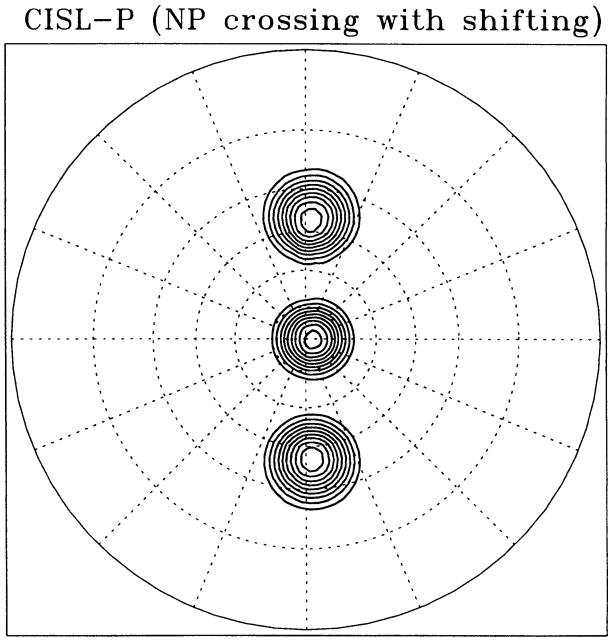

FIG. 6. Polar stereographic projection of the cosine bell advection over the north pole by the CISL-P scheme. (top) The positions of the cosine bell at time steps 32, 64, and 96 (from bottom to top of the frame). (bottom) As in the top panel but for the offset polar flow with $\alpha = \pi/2 - 0.05$.

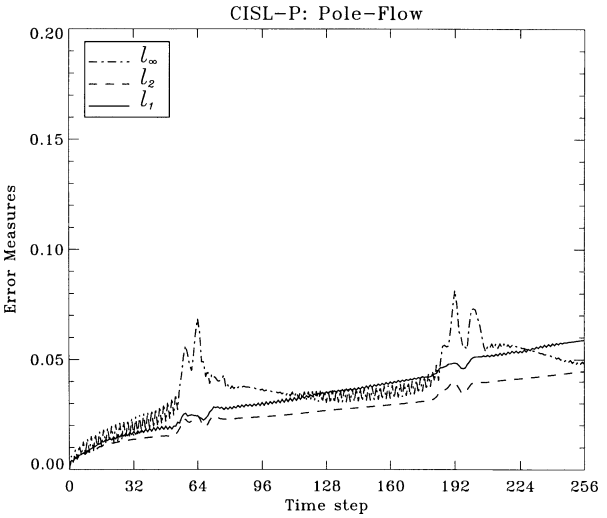

FIG. 7. Time traces of the normalized l_1, l_2, and l_∞ errors for the solid-body rotation test of the cosine bell, when the flow is along the pole-to-pole direction. The CISL-P scheme with 256 time steps is used for one revolution in the advection test.

from the corner points of the regular grid cells (the Eulerian cells) define the corner points of the departure cells. The sides in these so-called Lagrangian cells are generally defined as straight lines in a (λ, μ) plane. The mass distribution within each Eulerian grid cell is defined by quasi-biparabolic functions, which are used to integrate analytically the mass in each Lagrangian computational cell. The computational cells are auxiliary polygons, each with sides parallel to the coordinate axes and with the same area as the Lagrangian cell they approximate. They were introduced in order to simplify the analytical integrals of mass.

Near the poles the east and west sides of the Lagrangian cells cannot be approximated by straight lines in the (λ, μ) plane and are instead represented by straight lines in polar tangent plane coordinates. Each of these lines are divided in a certain number of equal pieces, the end points of which are transformed to the (λ, μ) plane. Thereby, the latitudinal belt of Lagrangian cells in the polar zones are split up into several latitudinal belts of subcells, which can be treated as the usual belts closer to the equator. One latitudinal belt in each hemisphere, the so-called singular belt, which enclose the Eulerian pole, is treated in a special way. Otherwise it would have required a special treatment of the singular cell enclosing the Eulerian pole and a subdivision in many subbelts of the whole singular belt. First the total mass in the singular belt is determined and then it is distributed among the cells in the belt using as weights values at the midpoints of the cells determined by a traditional SL scheme. By this procedure the total mass

TABLE 3. Error measures for solid-body rotation experiments when $\alpha = \pi/2$, with 72 time steps for one revolution. The traditional SL scheme with bicubic-Lagrange interpolation (SL-BCL) is used for comparison.

Scheme	l_1	l_2	l_∞	Mass	Max	Min
CISL-N	0.037	0.031	0.033	0	−0.028	−0.0034
CISL-P	0.034	0.029	0.033	0	−0.028	−0.0029
CISL-M	0.040	0.042	0.068	0	−0.024	−0.0004
SL-BCL	0.112	0.073	0.063	0.0023	−0.0047	−0.046

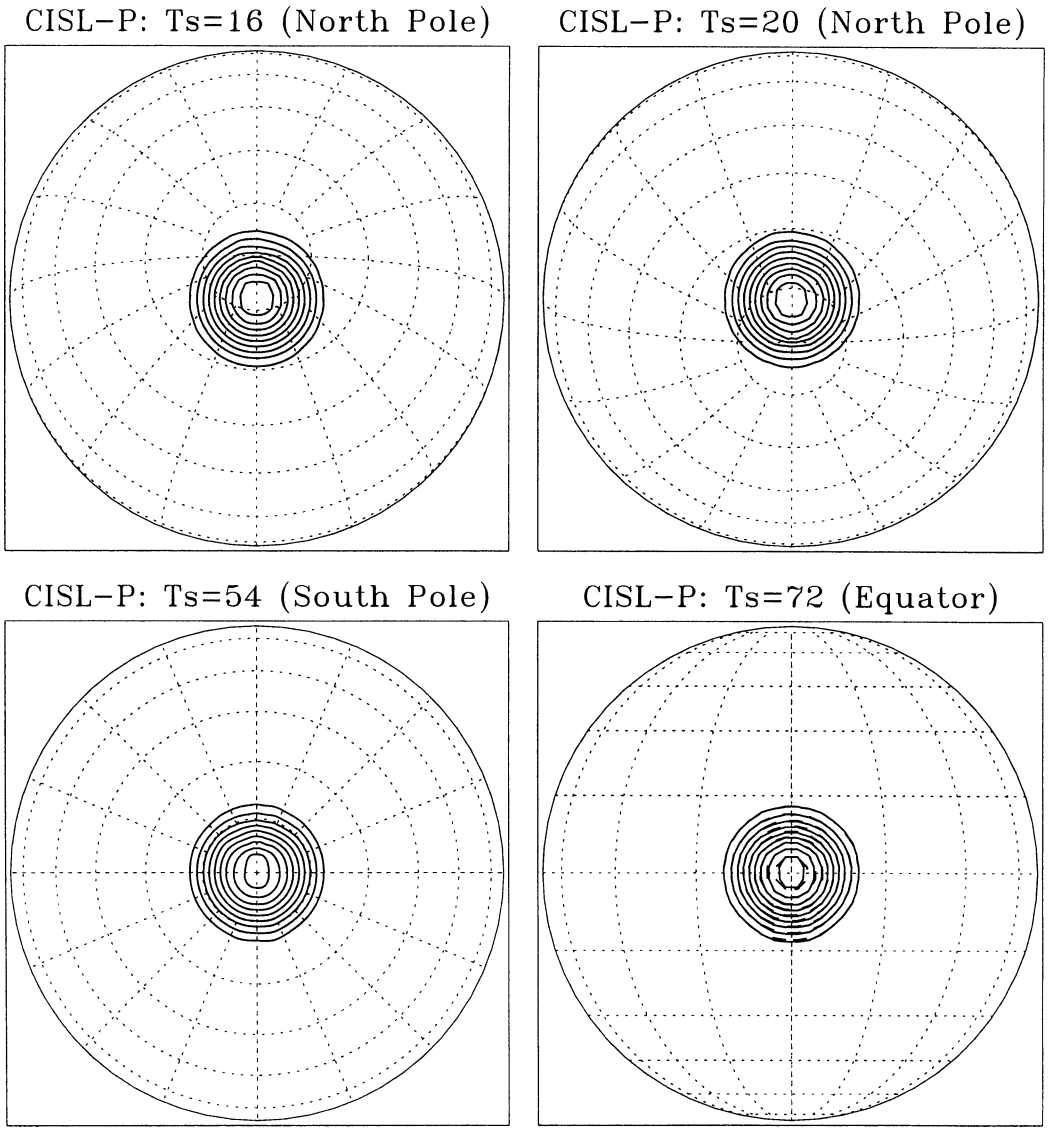

FIG. 8. Results on an orthographic projection of solid-body rotation of a cosine bell in the pole-to-pole direction. The number of time steps required for one revolution is 72, which corresponds to the directional Courant numbers $C_\lambda = 36.2$, $C_\theta = 1.78$. The CISL-P scheme is used for the advection. (top left), (top right) The position of the cosine bell as it passes over the north pole at time steps 16 and 20, respectively. (bottom left), (bottom right) The cosine bell over the south pole (at time step 54) and over the equator (after one revolution), respectively. The initial position (analytic solution) is marked by dashed contours.

is still conserved while the conservation for the individual cells in the singular belt is only approximately maintained. These special treatments in the polar caps fit well into the general program structure and can be implemented with only small modifications in the general code used for the rest of the sphere.

Compared to two other conservative advection schemes implemented on the sphere, LR96 and Rasch (1994), our CISL scheme was found to be competitive in terms of accuracy for the same resolution. In addition the CISL scheme has the advantage over these schemes that it is applicable for Courant numbers larger than one. Tests also showed that the polar cap treatments introduced here are relatively accurate. However, there is room for improvement in making advection over the poles as accurate as it is along the equator. Such an improvement is possible and may be achieved by extending the general procedure we have used near the poles to the singular belt, that is, by introducing a sufficient number of auxiliary points for dividing the Lagrangian cells in the singular belts. Then mass in the singular cells may be determined separately by a procedure similar to the one used in the present study for the whole singular belts. Together with the so-called reduced grid system (Rasch 1994), this might be just as efficient as the simple approach introduced above.

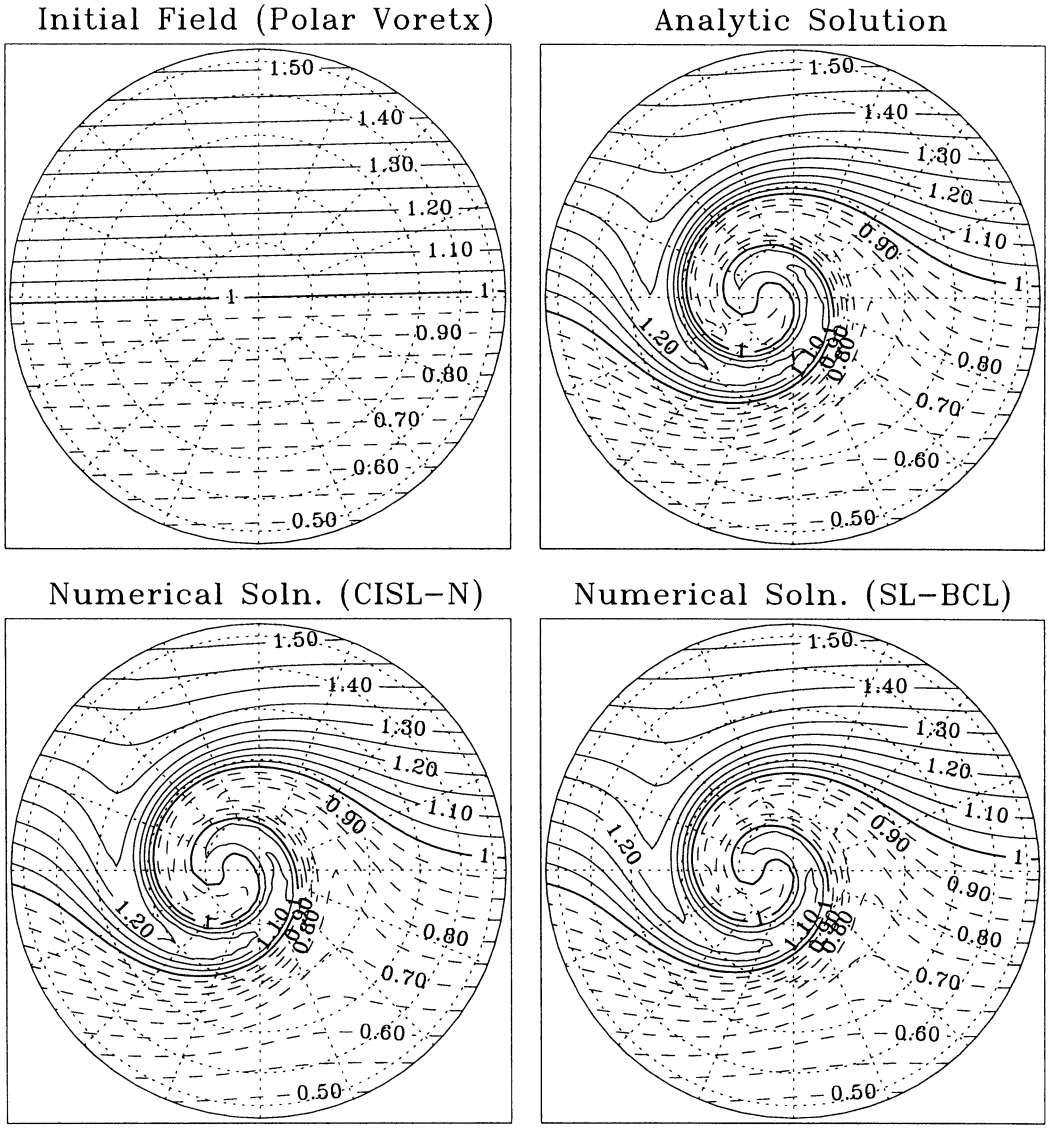

FIG. 9. Results of a polar vortex simulation over the sphere. The vortex center is located near the pole. (top left) The initial field and (top right) analytic solution after three nondimensional time units. (bottom left) The numerical solution simulated by the CISL scheme without any filter (CISL-N), and (bottom right) simulated field when using the traditional SL scheme with bicubic-Lagrange interpolation. For the numerical integrations, 32 time steps are used.

Computational efficiency is an important issue for transport schemes. The algorithm presented here has not been optimized to reduce the computational cost. Nevertheless, we have compared the performance of our CISL scheme with the traditional SL scheme based on bicubic-Lagrange interpolation (SL-BCL). Considering at first Cartesian coordinates in a plane, the cell method developed by Rančić (1992) had been shown to be very accurate as compared to the SL-BCL scheme. However, the scheme took approximately 2.5 as much computa-

TABLE 4. Error measures for polar vortex simulation test using CISL schemes and the SL-BCL scheme. For numerical integration 32 time steps are used (three time units).

Scheme	l_1	l_2	l_∞	Mass	Max	Min
CISL-N	0.0011	0.0025	0.0144	0	-6.4×10^{-5}	-1.9×10^{-5}
CISL-P	0.0011	0.0025	0.0144	0	-6.4×10^{-5}	-1.9×10^{-5}
CISL-M	0.0013	0.0031	0.0211	0	-8.1×10^{-5}	5.2×10^{-5}
SL-BCL	0.0072	0.0142	0.0513	0.0002	1.4×10^{-6}	6.9×10^{-7}

tional time as that of the SL scheme. We have done a similar experiment for solid-body rotation of a slotted cylinder (Nair et al. 1999a) on a uniform-resolution grid. Our CISL scheme takes approximately 1.1 as much computational time as that of the SL-BCL scheme, the accuracy of the solution is much better than that of SL-BCL, and it is comparable to the numerical solution produced by an SL scheme with cubic spline interpolation (Nair et al. 1999a).

In the spherical domain our CISL scheme is slightly more expensive, mainly due to the additional computational requirement in the polar caps. For the solid-body rotation experiment over the sphere, we found that the CISL scheme takes approximately 1.28 as much computational time as the SL-BCL scheme does. However, in addition to conserving the mass exactly, which the SL-BCL does not, the accuracy of the CISL scheme is superior. This overhead of 28% may be reduced with optimized codes, but even if it is not reduced, it seems to be a reasonable price to pay for the increased accuracy, including exact mass conservation. Concerning memory requirements in the CISL remapping scheme we note that, in addition to the coefficients of the quasi-biparabolic function, accumulated coefficients need to be stored along the latitudinal direction. Also the indices of the departure points need to be stored as this cell information can be shared for all fields to be advected at any time step. An optimized way of coding could, however, significantly reduce the memory requirement.

In the present study we have concentrated on a CISL scheme for 2D advection only. A perspective for the future is, however, a consistent extension of that scheme to a conservative 3D advection scheme (Machenhauer and Olk 1998), which may be applied in all the advection terms in a global multilevel PE numerical model and be combined with the semi-implicit time-stepping scheme (Machenhauer and Olk 1997).

Acknowledgments. The main part of the present study was carried out when both authors were employed at the Max Planck Institute for Meteorology, Hamburg, Germany. We thank Prof. Lennart Bengtsson for his support during the course of this work. The first author would like to thank the North Carolina Supercomputing Center for additional computer time.

REFERENCES

Bott, A., 1993: The monotone area-preserving flux-form advection algorithm: Reducing the time-splitting error in two-dimensional flow fields. *Mon. Wea. Rev.,* **121,** 2638–2641.

Carpenter, R. L., K. K. Droegemeier, P. R. Woodward, and C. E. Hane, 1990: Application of the piecewise parabolic method (PPM) to meteorological modeling. *Mon. Wea. Rev.,* **118,** 586–612.

Colella, P., and P. R. Woodward, 1984: Piecewise parabolic method for gas-dynamical simulations. *J. Comput. Phys.,* **54,** 174–201.

Côté, J., S. Gravel, A. Methot, A. Patoine, M. Roch, and A. Staniforth, 1998: The operational CMC/MRB Global Environmental Multiscale (GEM) model. *Mon. Wea. Rev.,* **126,** 1373–1395.

Doswell, C. A., 1984: A kinematic analysis of fromtogenesis associated with a nondivergent vortex. *J. Atmos. Sci.,* **41,** 1242–1248.

Dukowicz, J. K., 1984: Conservative rezoning (remapping) for general quadrilateral meshes. *J. Comput. Phys.,* **54,** 411–424.

Gravel, S., and A. Staniforth, 1994: A mass-conserving semi-Lagrangian scheme for shallow-water equations. *Mon. Wea. Rev.,* **122,** 243–248.

Hourdin, F., and A. Armengaud, 1999: The use of finite-volume methods for atmospheric advection of trace species. Part I: Test of various formulation in a general circulation model. *Mon. Wea. Rev.,* **127,** 822–837.

Laprise, J. P. R., and A. Plante, 1995: A class of semi-Lagrangian integrated-mass (SLIM) numerical transport algorithms. *Mon. Wea. Rev.,* **123,** 553–565.

Leslie, L. M., and R. J. Purser, 1995: Three dimensional mass-conserving semi-Lagrangian schemes employing forward trajectories. *Mon. Wea. Rev.,* **123,** 2551–2566.

Li, Y., and J. S. Chang, 1996: A mass-conservative, positive-definite, and efficient Eulerian advection scheme in spherical geometry and on a nonuniform grid system. *J. Appl. Meteor.,* **35,** 1897–1913.

Lin, S.-J., and R. B. Rood, 1996: Multidimensional flux-form semi-Lagrangian transport schemes. *Mon. Wea. Rev.,* **124,** 2064–2070.

Machenhauer, B., and M. Olk, 1996: On the development of a cell-integrated semi-Lagrangian shallow water model on the sphere. *Proc. Workshop on Semi-Lagrangian Methods,* Reading, United Kingdom, ECMWF, 213–228.

——, and ——, 1997: The implementation of the semi-implicit scheme in cell-integrated semi-Lagrangian models. *Atmos.–Ocean,* **35,** 103–126.

——, and ——, 1998: Design of a semi-implicit cell-integrated semi-Lagrangian model. Max Planck Institute for Meteorology Tech. Rep. 265, Hamburg, Germany, 76–85.

Moorthi, S., R. W. Higgins, and J. R. Bates, 1995: A global multilevel atmospheric model using a vector semi-Lagrangian finite difference scheme. Part II: Version with physics. *Mon. Wea. Rev.,* **123,** 1523–1541.

Nair, R., J. Côté, and A. Staniforth, 1999a: Monotonic cascade interpolation for semi-Lagrangian advection. *Quart. J. Roy. Meteor. Soc.,* **125,** 197–212.

——, ——, and ——, 1999b: Cascade interpolation for semi-Lagrangian advection over the sphere. *Quart. J. Roy. Meteor. Soc.,* **125,** 1445–1468.

Prather, M. J., 1986: Numerical advection by conservation of second-order moments. *J. Geophys. Res.,* **91,** 6671–6681.

Priestley, A., 1993: A quasi-conservative version of semi-Lagrangian advection scheme. *Mon. Wea. Rev.,* **121,** 621–629.

Rančić, M., 1992: Semi-Lagrangian piecewise biparabolic scheme for two-dimensional horizontal advection of a passive scalar. *Mon. Wea. Rev.,* **120,** 1394–1406.

——, 1995: An efficient, conservative, monotone remapping for semi-Lagrangian transport algorithms. *Mon. Wea. Rev.,* **123,** 1213–1217.

Rasch, P. J., 1994: Conservative shape-preserving two-dimensional transport on a spherical reduced grid. *Mon. Wea. Rev.,* **122,** 1337–1350.

——, 1998: Recent development in transport schemes at NCAR. Max Planck Institute for Meteorology Tech. Rep. 265, Hamburg, Germany, 65–75.

Ritchie, H., C. Temperton, A. Simmons, M. Hortal, T. Davies, D. Dent, and M. Hamrud, 1995: Implementation of the semi-Lagrangian method in a high-resolution version of the ECMWF forecast model. *Mon. Wea. Rev.,* **123,** 489–514.

Scroggs, J. S., and F. H. M. Semazzi, 1995: A conservative semi-Lagrangian method for multi-dimensional applications. *Numerical Methods for Partial Differential Equations,* Vol. 11, John Wiley & Sons, 445–452.

Smolarkiewicz, P. K., and P. J. Rasch, 1991: Monotone advection on the sphere. *J. Atmos. Sci.,* **48,** 793–810.

——, and J. A. Pudykiewicz, 1992: A class of semi-Lagrangian approximations for fluids. *J. Atmos. Sci.*, **49,** 2082–2096.

Williamson, D. L., and P. Rasch, 1989: Two-dimensional semi-Lagrangian transport with shape preserving interpolation. *Mon. Wea. Rev.*, **117,** 102–129.

——, and J. G. Olson, 1998: A comparison of semi-Lagrangian and Eulerian polar climate simulations. *Mon. Wea. Rev.*, **126,** 991–1000.

——, J. B. Drake, J. Hack, R. Jacob, and P. N. Swartztrauber, 1992: A standard test for numerical approximation to the shallow water equations in spherical geometry. *J. Comput. Phys.*, **102,** 211–224.